ADVANCED ELECTRONIC MATERIALS
www.advelectronicmat.de

Nanoimaging of Electronic Heterogeneity in Bi_2Se_3 and Sb_2Te_3 Nanocrystals

Xiaowei Lu, Omar Khatib, Xutao Du, Jiahua Duan, Wei Wei, Xianli Liu, Hans A. Bechtel, Fausto D'Apuzzo, Mingtao Yan, Alexander Buyanin, Qiang Fu, Jianing Chen, Miquel Salmeron, Jie Zeng, Markus B. Raschke,* Peng Jiang,* and Xinhe Bao**

Topological insulators (TIs) are quantum materials with topologically protected surface states surrounding an insulating bulk. However, defect-induced bulk conduction often dominates transport properties in most TI materials, obscuring the Dirac surface states. In order to realize intrinsic topological insulating properties, it is thus of great significance to identify the spatial distribution of defects, understand their formation mechanism, and finally control or eliminate their influence. Here, the electronic heterogeneity in polyol-synthesized Bi_2Se_3 and chemical vapor deposition-grown Sb_2Te_3 nanocrystals is systematically investigated by multimodal atomic-to-mesoscale resolution imaging. In particular, by combining the Drude response sensitivity of infrared scattering-type scanning near-field optical microscopy with the work-function specificity of mirror electron microscopy, characteristic mesoscopic patterns are identified, which are related to carrier concentration modulation originating from the formation of defects during the crystal growth process. This correlative imaging and modeling approach thus provides the desired guidance for optimization of growth parameters, crucial for preparing TI nanomaterials to display their intrinsic exotic Dirac properties.

1. Introduction

Albeit traditional thermoelectric materials,[1,2] Bi_2Se_3, Sb_2Te_3, and Bi_2Te_3 have recently attracted resurgent attention following the discovery of their 3D topological insulating behavior,[3–5] featuring metallic surface states surrounding an insulating bulk. The associated unique electronic structure of the helical Dirac surface states results in many exotic physical properties, such as the topological magneto-electric effect,[6] Majorana fermions,[7] and the quantum anomalous Hall effect.[8] However, because of the low formation energy of intrinsic defects,[9] the resulting bulk conductivity often obscures or even suppresses the desired TI behavior.[10–12]

The realization of these novel topological phases requires high-quality TI thin films with sufficiently low defect concentration, typically obtained by molecular beam epitaxy growth.[13] Chemical vapor deposition (CVD) and polyol methods, which offer facile and cost-effective synthetic routes promising for large-scale device applications, have also received interest with successful demonstrations of the ambipolar field effect,[14] Aharonov–Bohm,[15,16] and Shubnikov-de Hass[17] oscillations in $(Bi_xSb_{1-x})_2Te_3$ nanoplates, as well as in Bi_2Se_3 and Be_2Te_3 nanoribbons. Nevertheless, the quantum Hall effect as a hallmark of Dirac surface states[18] has not yet been realized in these TI nanostructures. One possible reason might be the appreciable bulk conduction associated with

X. W. Lu, W. Wei, M. T. Yan, Prof. Q. Fu, Prof. P. Jiang, Prof. X. H. Bao
State Key Laboratory of Catalysis
CAS Center for Excellence in Nanoscience
Dalian Institute of Chemical Physics
Chinese Academy of Sciences
457 Zhongshan Road, Dalian 116023, China
E-mail: pengjiang@dicp.ac.cn; xhbao@dicp.ac.cn

X. W. Lu, J. H. Duan, M. T. Yan
University of Chinese Academy of Sciences
Beijing 100049, China

Dr. O. Khatib, Prof. M. B. Raschke
Department of Physics
Department of Chemistry and JILA
University of Colorado
Boulder, CO 80309, USA
E-mail: Markus.Raschke@colorado.edu

X. T. Du, X. L. Liu, Prof. J. Zeng
Hefei National Laboratory for Physical Sciences at the Microscale
University of Science and Technology of China
96 Jin Zhai Road, Hefei 230026, China
E-mail: zengj@ustc.edu.cn

J. H. Duan, Prof. J. N. Chen
Beijing National Laboratory for Condensed Matter Physics
Institute of Physics
Chinese Academy of Sciences
Beijing 100190, China

Dr. H. A. Bechtel, Dr. F. D'Apuzzo
Advanced Light Source
Lawrence Berkeley National Laboratory
Berkeley, CA 94720, USA

Dr. A. Buyanin, Prof. M. Salmeron
Materials Sciences Division
Lawrence Berkeley National Laboratory
Berkeley, CA 94720, USA

DOI: 10.1002/aelm.201700377

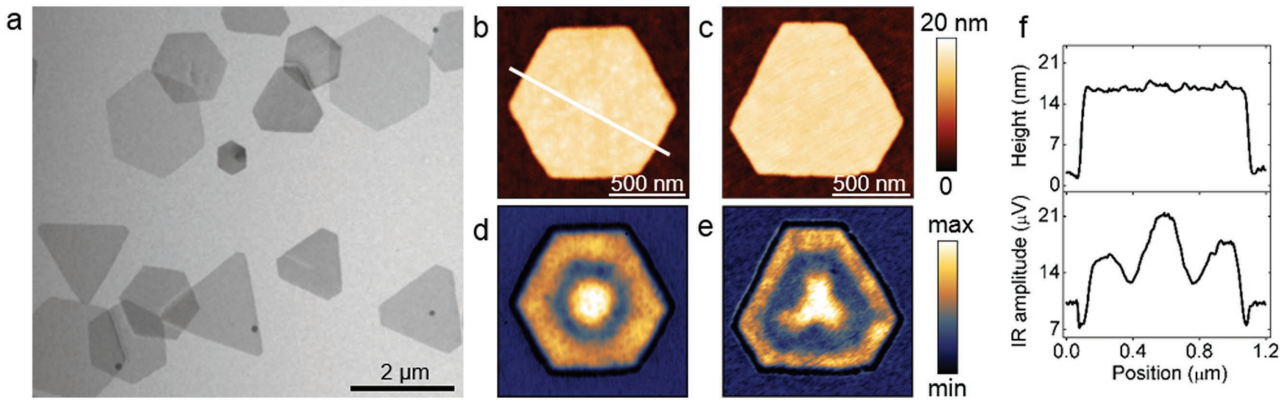

Figure 1. Structure and optical characterization of Bi_2Se_3 nanocrystals. a) Representative large-scale TEM image. Topographic b,c) and corresponding s-SNOM amplitude d,e) images of two individual Bi_2Se_3 nanocrystals drop-casted onto the SiO_2/Si substrates with incident infrared wavelength of 977 cm^{-1}. f) Line profiles taken from (b) and (d), respectively.

intrinsic defects formed during synthesis. In order to further explore the exotic quantum phenomenon of Dirac states in TI nanostructures, it is of great significance to probe, understand, and control the influence of doping, impurities, and defects on the local electronic structure of TI nanomaterials.

Scanning tunneling microscopy (STM) has been used to identify the individual vacancies and dopants at the atomic scale.[9,19–21] However, STM is limited to conducting substrates and typically cannot access heterogeneity that spans the multiple atomic-to-mesoscopic length scales. Infrared scattering-type scanning near-field optical microscopy (IR s-SNOM), in contrast, based on an atomic force microscope (AFM) coupled with a tip-localized optical excitation, can probe the low-energy local electronic structure associated with the Drude response with 10 nm resolution, and over multiple length scales with exquisite sensitivity.[22–24] Up to now, no comprehensive combined synthesis and multimodal atomic-to-mesoscale imaging approach has yet been performed to address the distribution of defects and its influence on the electronic and optical properties.

In this work, we performed multimodal nanoimaging and -spectroscopy combining the virtues of IR s-SNOM with a range of electron and X-ray-based imaging and chemical nanoanalysis methods, including mirror electron microscopy (MEM), nano-Auger, transmission electron microscopy (TEM), and energy-dispersive X-ray spectroscopy (EDX), to map the heterogeneity in optical response, defects, and chemical composition of Bi_2Se_3 nanocrystals synthesized by a polyol method. Remarkably, IR s-SNOM reveals highly symmetric nano-optical patterns in Bi_2Se_3 nanocrystals, whereas there is no corresponding contrast in generally used characterization methods, including AFM topography, TEM, and EDX elemental mapping. Further corroborated by theoretical simulation and MEM, which has the ability to measure the local work function variation,[25] we attribute the observed near-field contrast to the heterogeneity in carrier concentration. We also observed similar optical inhomogeneities in CVD-grown Sb_2Te_3 system. By comparing and analyzing the two different preparation methods, we propose that, for the synthesis of TI nanostructures, intrinsic defects tend to form during both the nucleation and subsequent cooling stages. Although their amount might be too tiny to be detected by traditional techniques, their influence on the electronic and optical properties is significant. Therefore, our findings have important implications for defect engineering and realization of intrinsic quantum phenomena in TIs and related 2D materials.

2. Results and Discussion

Figure 1a displays a representative TEM image of polyol-synthesized Bi_2Se_3 nanocrystals, and Figure 1b–e shows simultaneously acquired topographic and s-SNOM amplitude images for 977 cm^{-1} laser excitation of two individual Bi_2Se_3 nanocrystals on a SiO_2/Si substrate. The regular shapes, uniform mass-thickness contrast, and nearly atomically flat height determined from the TEM (Figure 1a) and AFM (Figure 1b,c,f) measurements indicate high crystalline quality of the Bi_2Se_3 nanocrystals. However, near-field infrared measurements (Figure 1d,e) of these samples intriguingly reveal a regular mesoscopic heterogeneity, which is not observed in exfoliated Bi_2Se_3 flakes.[26] The nanocrystal in Figure 1d exhibits a wide bright edge with a regular bright round center, whereas the nanocrystal in Figure 1e has a narrower bright edge with a three-fold symmetric center. As shown in a large-scale s-SNOM image (15 μm × 15 μm) of multiple nanocrystals (Figure S1, Supporting Information), the distinct near-field contrast is present in most of these nanocrystals. It is worth emphasizing that these patterns differ from the optical contrast in Sb_2Te_3 platelets reported in previous studies.[27] There, the pattern is closely related to the spiral growth, with a topographically rough surface with screw dislocations, whereas in our system, the surface is flat, with no association of a screw dislocation with the formation of the optical patterns.

IR s-SNOM image contrast can be related to a variety of physical properties, such as surface plasmons,[28,29] phonon polaritons,[30–32] or variations in local carrier concentration associated with defects, doping, or impurities.[27,33,34] Considering that IR s-SNOM is sensitive to low-energy intra- and interband transitions, Drude conductivity, and related surface excitations, we performed broadband spectroscopic nanoimaging using synchrotron near-field infrared nanospectroscopy (SINS)[35] from 750 to 2000 cm^{-1}. **Figure 2**b shows a spectrally integrated

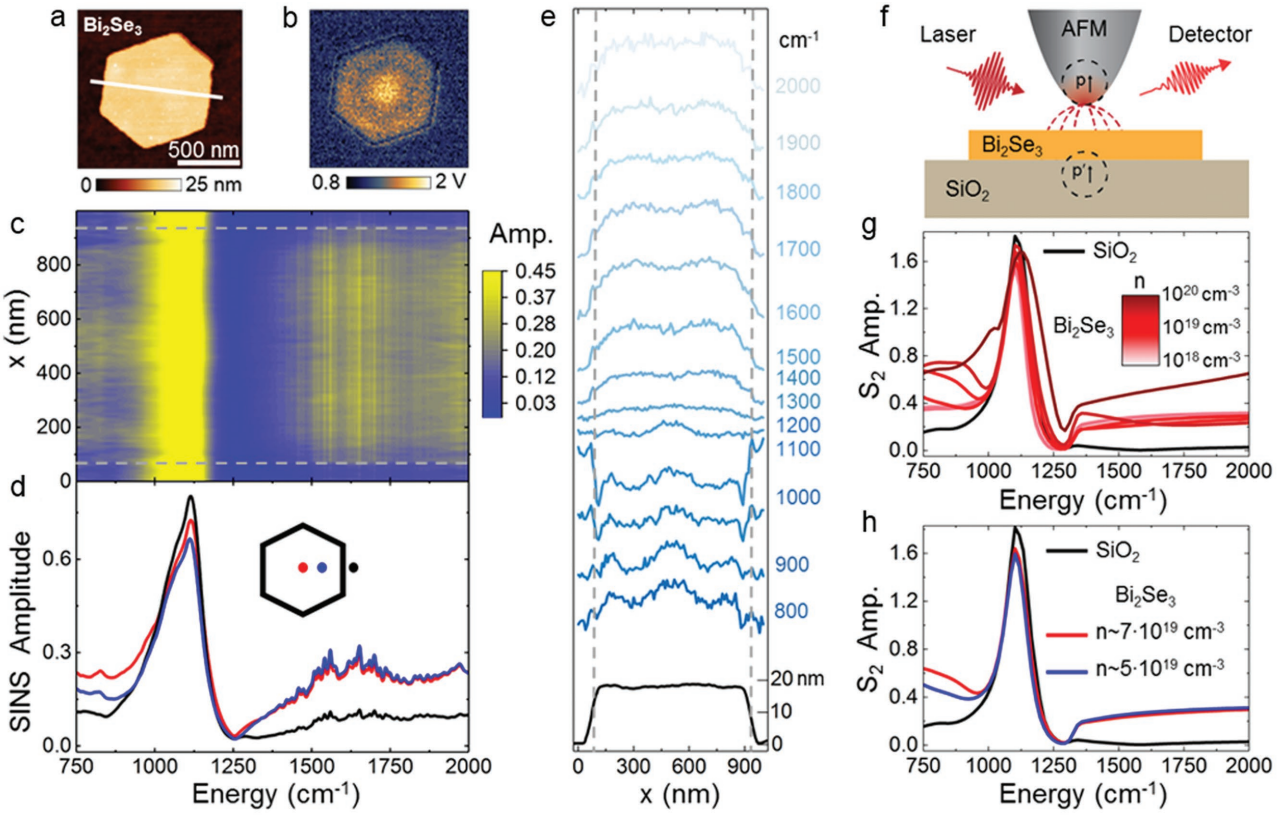

Figure 2. SINS of a Bi_2Se_3 nanocrystal on a SiO_2/Si substrate and the simulation of the interaction between SiO_2 and Bi_2Se_3 with different carrier concentrations. AFM topography a) and spectrally integrated broadband SINS image b). c) SINS line scan showing near-field amplitude along the white line in (a). d) Representative SINS spectra, at locations marked by colored circles in inset, showing varying near-field spectral behavior for different positions both on nanocrystal and on substrate. e) Frequency line cuts (shaded blue lines) extracted from (c) at select energies, as indicated, together with the AFM height profile (black line). Dashed gray lines in (c) and (e) indicate nanocrystal edge. f) Schematic of tip–sample interaction for thin nanocrystal atop bulk substrate. g) Predicted s-SNOM amplitude S_2 (normalized to Au) using a modified point-dipole model for SiO_2 (black line), and a 15 nm thin Bi_2Se_3 nanocrystal on SiO_2 with variable carrier concentration (shaded red lines), where (h) shows the best match to the experimental data for carrier densities of $n = 5 \times 10^{19}$ cm^{-3} (blue line) and $n = 7 \times 10^{19}$ cm^{-3} (red line).

broadband SINS image of a Bi_2Se_3 nanocrystal on SiO_2/Si substrate (Figure 2a), revealing the same contrast observed in monochromatic s-SNOM image above (Figure 1d). To obtain the full near-field nanospectroscopic response, SINS spectra were collected at each pixel as the sample is scanned along the white line indicated in Figure 2a. The resulting SINS near-field amplitude as a function of sample position is displayed in Figure 2c. A pronounced signal peak near 1100 cm^{-1} characterizes the optical response, with distinct variation in intensity as a function of position below 1000 cm^{-1}, as well as an overall increase in signal at energies above 1500 cm^{-1}. These trends are more clearly seen in Figure 2d, where representative SINS spectra are shown for specific positions (the inset in Figure 2d). Figure 2e shows shaded color line profiles, corresponding to fixed frequency line cuts across the nanocrystal, obtained from data in Figure 2c. The probe depth of s-SNOM is determined by the degree of field localization at the tip apex to at most a few tens of nanometers. As the nanocrystals are typically only 7–20 nm in height, the spectral SINS response is dominated by the surface phonon polariton (SPhP) resonance (≈1108 cm^{-1}) of the SiO_2 substrate.[32] However, there are also significant variations in the SINS response across the nanocrystal (Figure 2c), with features absent in the substrate response (black line in Figure 2d), notably a position-dependent increase in overall SINS intensity at energies below the SiO_2 phonon.

Given the high crystal quality of Bi_2Se_3 and the dominant spectral signal from the SiO_2 SPhP, one might correlate the observed s-SNOM patterns to a near-field excitation of SPhPs in the SiO_2 substrate. In such a system, these tip- and/or crystal edge-excited surface modes propagate at the interfaces and interfere with each other, giving rise to periodic variations in the s-SNOM signal with a pronounced frequency dependence. However, for the case of a thin dielectric, the existence of these modes is confined only to the frequency range within the reststrahlen band of the substrate, when the dielectric function becomes negative, as was recently demonstrated for phase change materials on quartz (1070–1230 cm^{-1}).[32] As seen in both monochromatic s-SNOM images taken at different illumination wavelengths (Figure S2, Supporting Information) and the line cuts extracted from the SINS line scan (Figure 2e), the optical patterns in Bi_2Se_3/SiO_2/Si exist in a rather wide frequency range. Further, given the much weaker dielectric response of thermally grown SiO_2 compared with crystalline quartz, we do not anticipate the existence of polariton modes

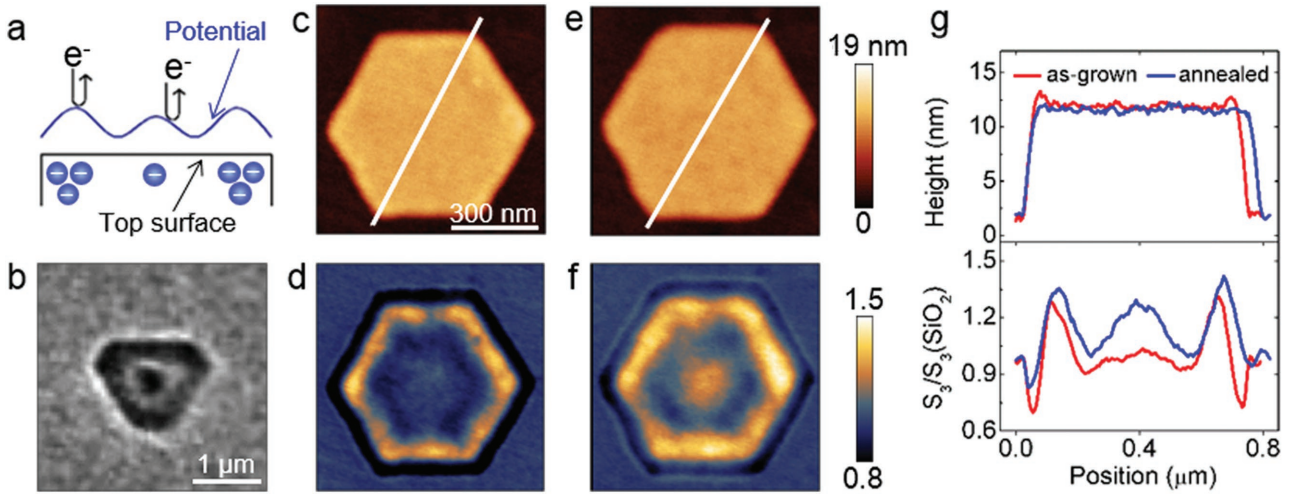

Figure 3. Identification of the origin of the observed optical contrast on Bi_2Se_3 nanocrystals. a) Schematic of the interaction between the incident electrons and the surface potential above the sample in MEM. b) MEM image of a Bi_2Se_3 nanocrystal on Si substrate. Topography (c) and s-SNOM amplitude image (d) of an as-grown Bi_2Se_3 nanocrystal. Topography (e) and s-SNOM amplitude image (f) of the same nanoplate in (c) annealed at 350 °C for 30 min under argon protection. The illumination wavelength was 937 cm^{-1}. The laser power was kept the same during the s-SNOM characterization, and the obtained s-SNOM amplitudes were normalized to that of the SiO_2/Si substrate for comparison. g) Line profiles taken from (c–f), respectively.

at interfaces with high-index materials such as Bi_2Se_3. Last, even replacing the SiO_2 substrate with Si (native oxide etched by HF), the optical pattern still persists (Figure S3, Supporting Information). Thus, SiO_2 phonon-related SPhPs are insufficient to explain the observed spatial variations.

Instead, our IR s-SNOM results can be well explained by a local variation of carrier concentration. The IR s-SNOM response of doped Bi_2Se_3 nanocrystals on SiO_2 can be described qualitatively based on a simplified point dipole model, which is employed to approximate the AFM tip–sample interaction to first order.[36] Here, the AFM tip is represented by an oscillating dipole induced by the laser field, as illustrated in Figure 2f. The tip-scattered radiation then contains contributions from both the far-field Fresnel scattering of the tip and sample surface reflection, as well as the local tip–sample near-field interaction, which encodes the sample properties. The simple dipole model for s-SNOM often adequately describes the response of bulk materials, but must be modified to account for thin films or nanocrystals[37–40] (see Supporting Information for details). Here, we consider a two-layer system consisting of bulk SiO_2, modeled in the spectral region of interest as a Lorentzian oscillator centered at $\omega = 1060$ cm^{-1} (Figure S4a, Supporting Information), and a 15 nm thick Bi_2Se_3 layer with a moderate free carrier Drude response (Figure S4b, Supporting Information): $\sigma(\omega) = \frac{\sigma_{DC}}{1 - i\omega\tau}$, with $1/\tau$ as the scattering rate, and $\sigma_{DC} = \frac{4\pi n e^2 \tau}{m}$, where n is the bulk 3D carrier density, e is the electron charge, and m is the effective mass. Using typical values for Bi_2Se_3,[41,42] we fix $m = 0.14$ m_e and $1/\tau = 600$ cm^{-1}, and vary the carrier density to best fit the experimental trends seen in Figure 2d.

Figure 2g shows the simulated near-field amplitude results of our two-layer s-SNOM model for a range of doping, where we choose demodulation at the second harmonic of the tip to match our SINS measurements, and normalize to Au. Though overestimating the overall strength of the s-SNOM response, we find good qualitative agreement with our experimental data assuming carrier concentrations in the range of $5–7 \times 10^{19}$ cm^{-3} (Figure 2h). This order of magnitude is consistent with Hall measurements on drop-casted Bi_2Se_3 thin films and doping levels seen in previous studies of Bi_2Se_3 thin films.[42,43] The contrast is most pronounced for frequencies below 1000 cm^{-1}, also in agreement with imaging measurements. Furthermore, this result conforms to the expected behavior of the far-field reflectivity calculated for carrier densities ranging from 10^{18} to 10^{20} cm^{-3} within our experimental measurement range (Figure S4d, Supporting Information).

To further support that the observed near-field contrast is related to the local variation in carrier concentrations, we performed MEM characterizations on Bi_2Se_3 nanocrystals. In MEM, the incident electrons at very low energy deflect before reaching the sample surface, and only interact with its electrostatic potential, as illustrated in **Figure 3**a. The contrast in MEM primarily arises from the spatial variations of surface topography and work function.[25] Figure 3b shows a typical MEM image of a Bi_2Se_3 nanocrystal on a Si substrate. The contour of this nanocrystal is regular, i.e., truncated triangular, exhibiting a clear pattern analogous to the nano-optical s-SNOM pattern in Figure 1d. In view of most Bi_2Se_3 nanocrystals with a flat surface (Figure S1a, Supporting Information), the effect of nonuniform thickness on the MEM image contrast in Figure 3b can be ignored. As a result, based on the correlation between MEM and s-SNOM, local carrier concentration variations are recognized as the origin of the observed optical contrast.

To address the nature of the defects that lead to the variations in the local doping, we subsequently resort to the analysis of crystal structure and chemical composition by TEM, EDX, and nano-Auger elemental mapping. Selected area electron diffraction taken from different positions on a Bi_2Se_3 nanocrystal, with well-defined six-fold symmetric diffraction spots, verifies the single crystalline nature (Figure S5, Supporting Information). Moreover, crystallographic orientation within the

nanocrystal is uniform, verifying the absence of twinning and amorphous phases. For Bi_2Se_3, the most common defect is Se deficiency.[9] However, the EDX elemental mapping shows that Se and Bi are uniformly distributed within the detection limit of ≈0.5 wt% (Figure S6, Supporting Information). Even in nano-Auger element mapping (Figure S7, Supporting Information) with a lower detection limit (≈0.1 at%) and a higher lateral resolution (≈10 nm), the distribution of Se also appears to be uniform. It should be noted that nano-Auger is surface sensitive with a probing depth of 0.5–5 nm, while s-SNOM has sensitivity to depths of up to 50–100 nm and is not confined just to the surface (top few nanometers) of materials. According to a recent X-ray photoelectron spectroscopy study on Bi_2Se_3, the surface of Bi_2Se_3 can be oxidized rapidly.[44] We believe it is the existence of surface oxide layer that results in the inability of nano-Auger to detect the inhomogeneities revealed by s-SNOM. In the high-resolution TEM images (Figure S8, Supporting Information), we cannot observe obvious defects with regular distribution. Consequently, we propose that it is local point defects (i.e., Se vacancies) that are responsible for regions with different carrier concentrations, similar to the case observed in ZnO nanowires.[34]

This scenario is further confirmed by monitoring the evolution of optical properties of nanocrystal with thermal annealing treatment, which could induce extra defects by thermal decomposition. Figure 3c–f displays the topographic and s-SNOM amplitude images of an as-grown and post-annealed (350 °C for 30 min under argon protection) Bi_2Se_3 nanocrystal with thickness of 9.8 nm. After annealing, the height of Bi_2Se_3 nanocrystals does not change and the surface remains flat, suggesting that there is no distinct degradation (Figure 3g). Nevertheless, the infrared amplitude of the post-annealed nanocrystal exhibits an overall increase, especially around the core region (Figure 3f). This phenomenon can be understood considering that the core of synthesized nanocrystals has a relatively low degree of crystallinity,[45,46] which might result in the easier volatilization of Se due to the weaker atomic bonding. The formation of one Se vacancy is accompanied by the generation of two free electrons according to Kroger–Vink notation $Se_{Se} = V_{Se}^{\cdot\cdot} + Se(g) + 2e'$, where Se_{Se} refers to a Se^{2-} ion sitting on a Se lattice site, $V_{Se}^{\cdot\cdot}$ is a Se vacancy with +2 charge, and e' is an electron.[47] Therefore, the carrier density as well as the infrared amplitude of the core would increase dramatically. The next interesting question rising immediately is if the Se vacancies can be eliminated by annealing the nanocrystal under a Se atmosphere, similar to the recent work performed by Gao et al. on WTe_2 thin films.[48] We annealed the Bi_2Se_3 nanocrystals under Se atmosphere at 300 °C for 4 h, and distinct infrared contrast still can be observed (Figure S9, Supporting Information). As a result, we believe that for the polyol-synthesized Bi_2Se_3, Se vacancies cannot be easily eliminated by a post-annealing process.

To examine the generality of the observations in Bi_2Se_3 in terms of its mesoscopic heterogeneities, we further investigated CVD-grown Bi_2Se_3 and Sb_2Te_3 nanocrystals. The CVD-grown Bi_2Se_3 nanocrystals exhibit quite uniform optical contrast (Figure S10, Supporting Information), indicating that the observed infrared heterogeneity in polyol-synthesized Bi_2Se_3 is related to specific growth processes. Interestingly, for the Sb_2Te_3 nanocrystals on mica substrate, we also observed similar optical

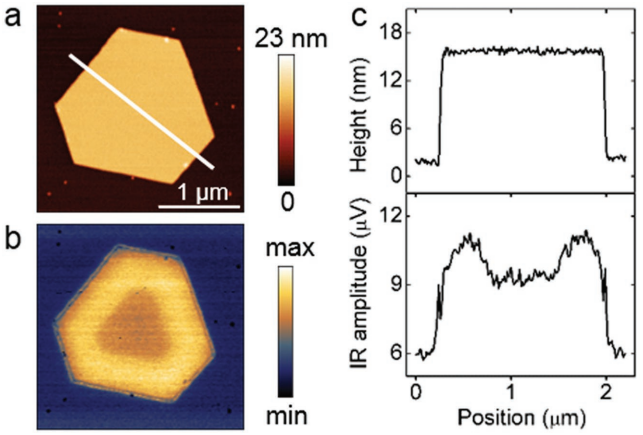

Figure 4. Optical inhomogeneity in CVD-grown Sb_2Te_3 nanocrystals. AFM topographic (a) and s-SNOM amplitude (b) images of Sb_2Te_3 nanocrystal on mica substrate. The illumination wavelength was 937 cm^{-1}. c) Line profiles taken from (a) and (b), respectively.

inhomogeneity using IR s-SNOM, which has no counterpart in the topography (**Figure 4**). Detailed infrared nanospectroscopy analysis can be found in Figure S11 in the Supporting Information. The optical contrast in most of the Sb_2Te_3 nanocrystals exhibits a dim center with a bright edge in IR s-SNOM images. It is noteworthy that a similar inhomogeneity pattern has been revealed on CVD-grown transition metal dichalcogenides (TMDCs), as seen in photoluminescence mapping,[49–52] which is attributed to chalcogen deficiencies during cooling[51] and local strain.[52] For the growth of Sb_2Te_3 nanocrystals, Sb_2Te_3 powders were used as the single precursor, with the dissociation according to $Sb_2Te_3(s) = SbTe(g) + 1/2Sb_2(g) + Te_2(g)$.[53] These gaseous molecules are then transferred downstream by the carrier gas and deposited on the substrate to grow nanocrystals. We propose that at the growth termination stage, after switching off the heat source, the growth does not stop immediately. Due to the reduced source supply, vacancy defects readily form around the edges, which are reflected as the optically bright edge in IR s-SNOM images. As for the difference in infrared behavior between CVD-grown Sb_2Te_3 and Bi_2Se_3, the dissociation species of Bi_2Se_3 are mainly BiSe and Se, and those of Sb_2Te_3 are Sb and Te existing in the form of elementary molecules.[53] From the standpoint of electronegativity, the chemical bond between Sb and Te is weaker compared with that between Bi and Se. Consequently, for CVD-grown Sb_2Te_3 nanocrystals, it is easier to form vacancy (V_{Sb}) and antisite (Sb_{Te}) defects.

Based on the valuable information obtained from CVD-grown Sb_2Te_3, the growth of polyol-synthesized Bi_2Se_3 can be divided into three steps: nucleation, growth, and termination. The round and three-fold symmetric cores (Figure 1d,e) form at the nucleation stage, while the diversity of optical patterns may be related to the supersaturation inhomogeneity in the solution.[54] For the three-bladed core in Figure 1e, we assume that the adjacent edges are facing slightly different degrees of supersaturation, resulting in the generation of the anisotropic structure. The formation of brighter edges (Figure 1d,e) likely experiences a process similar to that in the CVD-grown TMDCs and Sb_2Te_3. During the termination stage, more point defects form around the edges due to the deficiency of reactive species.

The facile formation of these intrinsic defects, like Sb and Se vacancies, originates from the low formation energy of defects, which has been evidenced by a combination of high-resolution STM and first-principles calculations.[9,19] However, these previous studies only focus on the identification of defects at the atomic level, without probing the distribution of these defects at the mesoscopic scale, and the associated influence on the electronic structures and optical properties. Herein, our IR s-SNOM images reveal that these defect-rich regions, with higher carrier concentrations, can form mesoscale optical contrast with high symmetry, and these optical responses can be understood and simulated by a simple theoretical model (Figure 2h).

As evident from the calculated spectra in Figure 2g, IR s-SNOM can serve as a powerful nanodiagnostic tool for optimizing nanocrystal growth parameters, given the high sensitivity to small changes in the local doping. However, despite adequately capturing all salient features of the SINS data in Figure 2d, our model still represents a simplified approximation to the true tip–sample interaction. In order to extract quantitative values from the s-SNOM contrast, a proper treatment of the evanescent wave interaction between the tip and sample is required, including the full momentum dependence of the sample response, as well as incorporating realistic tip geometries.[55,56] Additionally, use of a nonresonant substrate such as Si or Au will simplify the analysis.

3. Conclusion

In conclusion, we have demonstrated the existence of mesoscopic inhomogeneities in polyol-synthesized Bi_2Se_3 and CVD-grown Sb_2Te_3 nanocrystals using IR s-SNOM. With the assistance of MEM and theoretical calculations, we propose that the optical inhomogeneities are correlative with fluctuations in the local carrier concentration originating from intrinsic defects during synthesis. By comparing with recent studies on TMDCs, our results suggest that the electronic inhomogeneities might be a general growth-related phenomenon common to novel 2D materials. It is worth emphasizing that these small quantities of vacancies, although extremely important, have been largely overlooked due to the low sensitivity of traditional characterization methods, including TEM, EDX elemental mapping and nano-Auger microscopy. IR s-SNOM stands out as an extremely sensitive method to investigate the local electronic structures and optical properties of quantum materials.[23,24] Furthermore, our observations indicate that it will be of great significance to precisely control the stoichiometry of reactive species during the growth process for obtaining defect-free quantum materials with intrinsic exotic properties.

Experimental Section

Growth of Bi_2Se_3: The few-quintuple layer Bi_2Se_3 nanocrystals were prepared using a polyol method. $Bi(NO_3)_3{\cdot}5H_2O$ and Na_2SeO_3 were used as reactants, and ethylene glycol was used as solvent. Detailed growth parameters and structural characterization can be found in ref. [54].

Growth of Sb_2Te_3: Sb_2Te_3 nanocrystals were grown in a low-pressure horizontal tube furnace. Sb_2Te_3 powders (99.999%, Alfa Aesar) were used as the single precursor, which were placed at the hot center of the tube furnace. The substrate, i.e., freshly cleaved fluorophlogopite mica, was placed in the downstream region at a distance of about 11 cm from the source materials. Before the deposition, the tube was first evacuated to a base pressure less than 1 pa and purged with argon gas in order to reduce oxygen contamination. The furnace temperature was raised up to 500–510 °C at a rate of 10 °C min^{-1} with argon flow rate of 60–80 sccm, leading to total pressure of 34–44 pa. The furnace was held at the growth temperature for 2–5 min to achieve a reasonable amount of products deposited on the substrates, and then cooled down to room temperature.

s-SNOM Nanoimaging: A commercial scattering-type scanning near-field optical microscopy (NeaSNOM, Neaspec GmbH) was employed for single frequency nanoimaging. Continuous-wave quantum cascade lasers (Daylight solutions) and a CO_2 gas laser (Access laser) covering the wavelength range from 5 to 11.3 μm were used as the light source. During the measurements, the metalized AFM tip (NanoWorld Arrow NCPt) oscillating with a frequency of Ω (≈280 kHz), was illuminated by a focused p-polarized mid-infrared laser beam, and the elastically backscattered signal was demodulated at higher harmonics 3 Ω to fully eliminate the contribution of background. The amplitude S_3 and phase ϕ_3 of tip-scattered field were extracted by the Pseudo-heterodyne detection. In this work, the s-SNOM amplitude images are mainly used.

s-SNOM Nano-spectroscopy: For synchrotron infrared nano-spectroscopy (SINS), infrared radiation from ALS Beamline 5.4 was focused onto a metallized AFM tip operated in intermittent contact mode Ω (≈250 kHz). For laser-based nano-spectroscopy (see Supplement), we used a femtosecond tunable IR laser with ≈250 cm^{-1} bandwidth based on an optical parametric oscillator (OPO) with difference frequency generation (DFG) (A.P.E. GmbH, Berlin). Near-field signal was detected at a higher harmonic of the tapping frequency using lock-in demodulation. The tip-scattered near-field signal was combined with light from a reference arm and interferometrically detected with an HgCdTe detector. SINS was performed using an AFM (Innova, Bruker) modified for s-SNOM. Point spectra were measured interferometrically with a modified Fourier-transform infrared spectrometer (FTIR) (Nicolet 6700), collected as asymmetric interferograms that were Fourier transformed to produce near-field amplitude S_2 and phase ϕ_2 spectra. SINS line scans were performed at a spectral resolution of 16 cm^{-1}. Laser-based spectra were acquired using a commercial IR s-SNOM nano-spectroscopy system (nanoIR2-s, Anasys Instruments). All spectra were normalized to a bare Au substrate.

MEM: MEM was carried out in an Elmitec LEEM III system under ultrahigh vacuum. The electron gun potential was −20 kV, and the sample potential was −20 kV + Start voltage (STV). For MEM mode, the STV should be less than zero to insure that the electrons were reflected before hitting the sample surface. The STV used in Figure 3b is −1.1 V. The Bi_2Se_3 nanocrystals were drop casted onto a bare Si substrate for MEM measurements.

Nano-Auger Electron Microscopy: An Oxford/Omicron nano-Auger system was used to study the distribution of Se element in Bi_2Se_3 nanocrystals. The lateral resolution of this system was ≈10 nm, and the analysis depth was 0.5–5 nm. Its detection limit was ≈0.1 at%

Supporting Information

Supporting Information is available from the Wiley Online Library or from the author.

Acknowledgements

X.W.L., O.K., and X.T.D. contributed equally to this work. The authors thank Ernst Bauer for fruitful discussions. P.J. and J.C. acknowledge financial support from the National Key Research and Development Program of China (Grant No. 2016YFA0203500) and the National Natural Science Foundation of China (Grant No. 51290272 and 11474350).

Funding for M.B.R. was provided by U.S. Department of Energy, Office of Basic Sciences, Division of Material Sciences and Engineering, under Award No. DE-SC0008807. M.B.R. and O.K. acknowledge support from the NSF Science and Technology Center on Real-Time Functional Imaging under DMR-1548924 for SINS development. The Advanced Light Source is supported by the Director, Office of Science, Office of Basic Energy Sciences, of the U.S. Department of Energy under contract no. DE-AC02-05CH11231. O.K. acknowledges support from the ALS Postdoctoral Fellowship program. M.S. and A.B. were supported by the U.S. Department of Energy, F474 Office of Basic Sciences, Division of Material Sciences and Engineering, under contract No. DE-AC02-05CH11231.

Conflict of Interest

The authors declare no conflict of interest.

Keywords

correlated imaging, electronic heterogeneity, mirror electron microscopy, scanning near field optical microscopy, topological insulator

Received: August 13, 2017
Revised: October 18, 2017
Published online: December 11, 2017

[1] B. Poudel, Q. Hao, Y. Ma, Y. C. Lan, A. Minnich, B. Yu, X. A. Yan, D. Z. Wang, A. Muto, D. Vashaee, X. Y. Chen, J. M. Liu, M. S. Dresselhaus, G. Chen, Z. F. Ren, *Science* **2008**, *320*, 634.
[2] S. I. Kim, K. H. Lee, H. A. Mun, H. S. Kim, S. W. Hwang, J. W. Roh, D. J. Yang, W. H. Shin, X. S. Li, Y. H. Lee, G. J. Snyder, S. W. Kim, *Science* **2015**, *348*, 109.
[3] H. J. Zhang, C. X. Liu, X. L. Qi, X. Dai, Z. Fang, S. C. Zhang, *Nat. Phys.* **2009**, *5*, 438.
[4] Y. Xia, D. Qian, D. Hsieh, L. Wray, A. Pal, H. Lin, A. Bansil, D. Grauer, Y. S. Hor, R. J. Cava, M. Z. Hasan, *Nat. Phys.* **2009**, *5*, 398.
[5] Y. L. Chen, J. G. Analytis, J. H. Chu, Z. K. Liu, S. K. Mo, X. L. Qi, H. J. Zhang, D. H. Lu, X. Dai, Z. Fang, S. C. Zhang, I. R. Fisher, Z. Hussain, Z. X. Shen, *Science* **2009**, *325*, 178.
[6] X. L. Qi, T. L. Hughes, S. C. Zhang, *Phys. Rev. B* **2008**, *78*, 195424.
[7] L. Fu, C. L. Kane, *Phys. Rev. Lett.* **2008**, *100*, 096407.
[8] C. Z. Chang, J. S. Zhang, X. Feng, J. Shen, Z. C. Zhang, M. H. Guo, K. Li, Y. B. Ou, P. Wei, L. L. Wang, Z. Q. Ji, Y. Feng, S. H. Ji, X. Chen, J. F. Jia, X. Dai, Z. Fang, S. C. Zhang, K. He, Y. Y. Wang, L. Lu, X. C. Ma, Q. K. Xue, *Science* **2013**, *340*, 167.
[9] J. X. Dai, D. West, X. Y. Wang, Y. Z. Wang, D. Kwok, S. W. Cheong, S. B. Zhang, W. Wu, *Phys. Rev. Lett.* **2016**, *117*, 106401.
[10] D. X. Qu, Y. S. Hor, J. Xiong, R. J. Cava, N. P. Ong, *Science* **2010**, *329*, 821.
[11] D. Kim, S. Cho, N. P. Butch, P. Syers, K. Kirshenbaum, S. Adam, J. Paglione, M. S. Fuhrer, *Nat. Phys.* **2012**, *8*, 459.
[12] K. Hoefer, C. Becker, D. Rata, J. Swanson, P. Thalmeier, L. H. Tjeng, *Proc. Natl. Acad. Sci. U S A* **2014**, *111*, 14979.
[13] Y. Zhang, K. He, C. Z. Chang, C. L. Song, L. L. Wang, X. Chen, J. F. Jia, Z. Fang, X. Dai, W. Y. Shan, S. Q. Shen, Q. A. Niu, X. L. Qi, S. C. Zhang, X. C. Ma, Q. K. Xue, *Nat. Phys.* **2010**, *6*, 584.
[14] D. S. Kong, Y. L. Chen, J. J. Cha, Q. F. Zhang, J. G. Analytis, K. J. Lai, Z. K. Liu, S. S. Hong, K. J. Koski, S. K. Mo, Z. Hussain, I. R. Fisher, Z. X. Shen, Y. Cui, *Nat. Nanotechnol.* **2011**, *6*, 705.
[15] H. L. Peng, K. J. Lai, D. S. Kong, S. Meister, Y. L. Chen, X. L. Qi, S. C. Zhang, Z. X. Shen, Y. Cui, *Nat. Mater.* **2010**, *9*, 225.
[16] H. Pan, K. Zhang, Z. X. Wei, J. Wang, M. Han, F. Q. Song, X. F. Wang, B. G. Wang, R. Zhang, *Appl. Phys. Lett.* **2017**, *110*, 053108.
[17] F. X. Xiu, L. A. He, Y. Wang, L. N. Cheng, L. T. Chang, M. R. Lang, G. A. Huang, X. F. Kou, Y. Zhou, X. W. Jiang, Z. G. Chen, J. Zou, A. Shailos, K. L. Wang, *Nat. Nanotechnol.* **2011**, *6*, 216.
[18] Y. Xu, I. Miotkowski, C. Liu, J. F. Tian, H. Nam, N. Alidoust, J. N. Hu, C. K. Shih, M. Z. Hasan, Y. P. Chen, *Nat. Phys.* **2014**, *10*, 956.
[19] Y. P. Jiang, Y. Y. Sun, M. Chen, Y. L. Wang, Z. Li, C. L. Song, K. He, L. L. Wang, X. Chen, Q. K. Xue, X. C. Ma, S. B. Zhang, *Phys. Rev. Lett.* **2012**, *108*, 066809.
[20] H. Beidenkopf, P. Roushan, J. Seo, L. Gorman, I. Drozdov, Y. S. Hor, R. J. Cava, A. Yazdani, *Nat. Phys.* **2011**, *7*, 939.
[21] C. Parra, T. H. R. da Cunha, A. W. Contryrnan, D. Kong, F. Montero-Silva, P. H. R. Goncalves, D. D. Dos Reis, P. Giraldo-Gallo, R. Segura, F. Olivares, F. Niestemski, Y. Cui, R. Magalhaes-Paniago, H. C. Manoharan, *Nano Lett.* **2017**, *17*, 97.
[22] R. Hillenbrand, T. Taubner, F. Keilmann, *Nature* **2002**, *418*, 159.
[23] J. M. Atkin, S. Berweger, A. C. Jones, M. B. Raschke, *Adv. Phys.* **2012**, *61*, 745.
[24] M. K. Liu, A. J. Sternbach, D. N. Basov, *Rep. Prog. Phys.* **2017**, *80*, 014501.
[25] E. Bauer, *Rep. Prog. Phys.* **1994**, *57*, 895.
[26] S. E. Grefe, M. Tan, S. Derakhshan S, Y. Abate, *MRS Online Proc. Libr. Arch.* **2013**, *1557*, https://doi.org/10.1557/opl.2013.1043.
[27] B. Hauer, T. Saltzmann, U. Simon, T. Taubner, *Nano Lett.* **2015**, *15*, 2787.
[28] J. N. Chen, M. Badioli, P. Alonso-Gonzalez, S. Thongrattanasiri, F. Huth, J. Osmond, M. Spasenovic, A. Centeno, A. Pesquera, P. Godignon, A. Z. Elorza, N. Camara, F. J. G. de Abajo, R. Hillenbrand, F. H. L. Koppens, *Nature* **2012**, *487*, 77.
[29] Z. Fei, A. S. Rodin, G. O. Andreev, W. Bao, A. S. McLeod, M. Wagner, L. M. Zhang, Z. Zhao, M. Thiemens, G. Dominguez, M. M. Fogler, A. H. Castro Neto, C. N. Lau, F. Keilmann, D. N. Basov, *Nature* **2012**, *487*, 82.
[30] N. Ocelic, R. Hillenbrand, *Nat. Mater.* **2004**, *3*, 606.
[31] S. Dai, Z. Fei, Q. Ma, A. S. Rodin, M. Wagner, A. S. McLeod, M. K. Liu, W. Gannett, W. Regan, K. Watanabe, T. Taniguchi, M. Thiemens, G. Dominguez, A. H. C. Neto, A. Zettl, F. Keilmann, P. Jarillo-Herrero, M. M. Fogler, D. N. Basov, *Science* **2014**, *343*, 1125.
[32] P. N. Li, X. S. Yang, T. W. W. Mass, J. Hanss, M. Lewin, A. K. U. Michel, M. Wuttig, T. Taubner, *Nat. Mater.* **2016**, *15*, 870.
[33] J. M. Stiegler, A. J. Huber, S. L. Diedenhofen, J. G. Rivas, R. E. Algra, E. P. A. M. Bakkers, R. Hillenbrand, *Nano Lett.* **2010**, *10*, 1387.
[34] J. M. Stiegler, R. Tena-Zaera, O. Idigoras, A. Chuvilin, R. Hillenbrand, *Nat. Commun.* **2012**, *3*, 1131.
[35] H. A. Bechtel, E. A. Muller, R. L. Olmon, M. C. Martin, M. B. Raschke, *Proc. Natl. Acad. Sci. U S A* **2014**, *111*, 7191.
[36] R. Hillenbrand, F. Keilmann, *Phys. Rev. Lett.* **2000**, *85*, 3029.
[37] Z. Fei, G. O. Andreev, W. Z. Bao, L. F. M. Zhang, A. S. McLeod, C. Wang, M. K. Stewart, Z. Zhao, G. Dominguez, M. Thiemens, M. M. Fogler, M. J. Tauber, A. H. Castro-Neto, C. N. Lau, F. Keilmann, D. N. Basov, *Nano Lett.* **2011**, *11*, 4701.
[38] L. M. Zhang, G. O. Andreev, Z. Fei, A. S. McLeod, G. Dominguez, M. Thiemens, A. H. Castro-Neto, D. N. Basov, M. M. Fogler, *Phys. Rev. B* **2012**, *85*, 075419.

[39] J. Aizpurua, T. Taubner, F. J. de Abajo, M. Brehm, R. Hillenbrand, *Opt. Express* **2008**, *16*, 1529.
[40] B. Hauer, A. P. Engelhardt, T. Taubner, *Opt. Express* **2012**, *20*, 13173.
[41] K. W. Post, B. C. Chapler, L. He, X. F. Kou, K. L. Wang, D. N. Basov, *Phys. Rev. B* **2013**, *88*, 075121.
[42] H. L. Cao, J. F. Tian, I. Miotkowski, T. Shen, J. N. Hu, S. Qiao, Y. P. Chen, *Phys. Rev. Lett.* **2012**, *108*, 216803.
[43] C. Martin, V. Craciun, K. H. Miller, B. Uzakbaiuly, S. Buvaev, H. Berger, A. F. Hebard, D. B. Tanner, *Phys. Rev. B* **2013**, *87*, 201201.
[44] D. S. Kong, J. J. Cha, K. J. Lai, H. L. Peng, J. G. Analytis, S. Meister, Y. L. Chen, H. J. Zhang, I. R. Fisher, Z. X. Shen, Y. Cui, *ACS Nano* **2011**, *5*, 4698.
[45] F. Li, Y. Ding, P. X. Gao, X. Q. Xin, Z. L. Wang, *Angew. Chem., Int. Ed.* **2004**, *43*, 5238.
[46] W. Z. Wang, D. Long, Y. J. Liang, G. L. Zhang, B. Q. Zeng, Q. Y. He, *Langmuir* **2011**, *27*, 815.
[47] F. T. Huang, M. W. Chu, H. H. Kung, W. L. Lee, R. Sankar, S. C. Liou, K. K. Wu, Y. K. Kuo, F. C. Chou, *Phys. Rev. B* **2012**, *86*, 081104.
[48] M. Gao, M. H. Zhang, W. Niu, Y. Q. Chen, M. Gu, H. Y. Wang, F. Q. Song, P. Wang, S. C. Yan, F. Q. Wang, X. R. Wang, X. F. Wang, Y. B. Xu, R. Zhang, *Appl. Phys. Lett.* **2017**, *111*, 031906.
[49] H. R. Gutiérrez, N. Perea-López, A. L. Elías, A. Berkdemir, B. Wang, R. Lv, F. López-Urías, V. H. Crespi, H. Terrones, M. Terrones, *Nano Lett.* **2013**, *13*, 3447.
[50] X. L. Wang, Y. J. Gong, G. Shi, W. L. Chow, K. Keyshar, G. L. Ye, R. Vajtai, J. Lou, Z. Liu, E. Ringe, B. K. Tay, P. M. Ajayan, *ACS Nano* **2014**, *8*, 5125.
[51] W. Bao, N. J. Borys, C. Ko, J. Suh, W. Fan, A. Thron, Y. J. Zhang, A. Buyanin, J. Zhang, S. Cabrini, P. D. Ashby, A. Weber-Bargioni, S. Tongay, S. Aloni, D. F. Ogletree, J. Q. Wu, M. B. Salmeron, P. J. Schuck, *Nat. Commun.* **2015**, *6*, 7993.
[52] K. D. Park, O. Khatib, V. Kravtsov, G. Clark, X. D. Xu, M. B. Raschke, *Nano Lett.* **2016**, *16*, 2621.
[53] R. A. Abramovitch, *Reactive Intermediates*, Springer Science & Business Media, New York **1983**.
[54] X. L. Liu, J. W. Xu, Z. C. Fang, L. Lin, Y. Qian, Y. C. Wang, C. M. Ye, C. Ma, J. Zeng, *Nano Res.* **2015**, *8*, 3612.
[55] A. S. McLeod, P. Kelly, M. D. Goldflam, Z. Gainsforth, A. J. Westphal, G. Dominguez, M. H. Thiemens, M. M. Fogler, D. N. Basov, *Phys. Rev. B* **2014**, *90*, 085136.
[56] B. Y. Jiang, L. M. Zhang, A. H. C. Neto, D. N. Basov, M. M. Fogler, *J. Appl. Phys.* **2016**, *119*, 054305.

